The origin of the constant phase element behavior of Pt(111) near the potential of zero charge

Levey, K.J.; Fröhlich, N.L.; Hardt, S.; Kam, L.B.T. de; Koper, M.T.M.

ACS Electrochemistry

pubs.acs.org/electrochem
Article

The Origin of the Constant Phase Element Behavior of Pt(111) Near the Potential of Zero Charge

Katherine J. Levey,[+] Nicci L. Fröhlich,[+] Steffen Hardt, Lucas B.T. de Kam, and Marc T.M. Koper*

Cite This: ACS Electrochem. 2026, 2, 693−704

ABSTRACT: Despite the Pt(111)/$HClO_4$ interface being a model system in electrochemistry, its electric double-layer (EDL) behavior deviates significantly from classical models. In the double-layer region (0.40−0.60 V_{RHE}), electrochemical impedance spectroscopy reveals non-ideal capacitance behavior, which is best described by a constant phase element rather than an ideal capacitor. The extent of non-ideal capacitive behavior can be quantified using the CPE exponent (α), in which we observe two distinct regimes: a decrease at potentials away from the potential of zero charge (PZC), and a pronounced minimum at the PZC itself. To interpret these findings, we combine experimental data with two-dimensional numerical simulations solving the coupled Poisson−Nernst−Planck equations. Our findings show that non-ideal capacitive behavior at potentials away from the PZC arises from finite mass transport within the EDL and an inhomogeneous current/potential distribution across the disc electrode, which results from the cell and electrode geometry. The anomalous α minimum at potentials closer to the PZC is the result of a second potential-dependent variable, which we propose to be electrowetting that alters the geometry of the wetted edge of the disk electrode in the hanging meniscus configuration and therefore the corresponding local electric field. These results highlight the critical roles of cell geometry, edge effects, and electrolyte concentration in modulating frequency dispersion. This work provides new physical insights into capacitance dispersion at well-defined interfaces and lays the foundation for more accurate models of electrochemical systems involving confined geometries and interfacial heterogeneity.

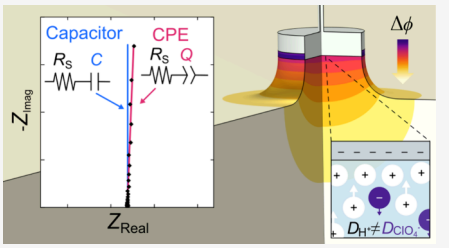

KEYWORDS: *electric double layer, constant phase element, impedance spectroscopy, Nernst−Planck−Poisson modeling, mass transport*

INTRODUCTION

Despite the importance of platinum as an excellent electrocatalyst, a fundamental understanding of its electric double layer (EDL) structure remains incomplete. This is a direct result of the fact that only the Pt(111) facet exhibits a "true double-layer window" between 0.40−0.60 V_{RHE} in the non-specifically adsorbing $HClO_4$ electrolyte where the surface is free of adsorbates.[1,2] All other facets of platinum do not exhibit adsorbate-free potential windows, owing to their greater affinity for H_2O dissociation.[3−6] As a result, chemical adsorption and electrostatic effects of EDL charging become convoluted, significantly complicating the direct understanding of their EDL structures.

While the Pt(111)/$HClO_4$ interface is considered a key, model system in electrochemistry,[1,2] it was previously revealed that this interface does not conform to current EDL models,[7,8] the most widely accepted of which is the Gouy-Chapman-Stern (GCS) model and its later theoretical extensions. The theory predicts a (differential) capacitance minimum, $C_{d,min}$, at the potential of zero charge (PZC, or the potential where the electrode surface has no excess free charge in a given electrolyte) which is dominated by the diffuse-layer capacitance (or the GC-capacitance, C_{GC}).[9,10] The PZC of Pt(111) in $HClO_4$ was previously found to be 0.30 V_{NHE} using other techniques,[11−14] meaning that on the reversible hydrogen electrode (RHE) scale, the PZC should be observable at pH's 2-4 (*i.e.*, the PZC is in the double-layer window).[15] However, Ojha *et al.* revealed that the GC-predicted $C_{d,min}$ can only be directly observed at very dilute concentrations of $HClO_4$, *i.e.*, pH 4, 0.1 mM.[7,8]

An interface behaves as an ideal capacitor when charge is stored by forming an electric field without resistive losses. However, using electrochemical impedance spectroscopy (EIS), we have previously found that the capacitance response in the double-layer window of the Pt(111)/$HClO_4$ interface does not behave ideally.[16] Instead, the capacitance is better modeled by an electrical equivalent circuit (EEC) consisting of a serially connected resistor (accounting for the solution resistance) and constant phase element (CPE, Q) as opposed to an ideal capacitor. The impedance of a CPE is given by

$$Z_{CPE} = \frac{1}{Q(j\omega)^{\alpha}} \quad (1)$$

Received: November 13, 2025
Revised: December 18, 2025
Accepted: December 24, 2025
Published: January 29, 2026

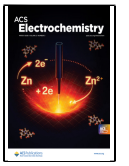

where ω is the angular frequency and α is the CPE exponent varying between 0 (purely resistive) and 1 (purely capacitive).[17] In this way, α quantifies the extent of non-ideality of the capacitance response, where values of $0.8 < \alpha < 1$ are considered non-ideal capacitances. In Nyquist impedance plots, CPE behavior can be readily observed as a straight line that is tilted relative to the real impedance (Z_{Real}) axis by an angle of $\alpha \times 90°$. Interestingly, we previously found that α exhibits a minimum at the PZC of Pt(111), which contradicts the expectation that the most ideal capacitance behavior would be expected at the PZC.[16] Importantly, such a minimum in α was also observed at higher electrolyte concentrations (1 mM $HClO_4$, pH 3) where no corresponding capacitance minimum could be observed using either CV or EIS, in turn suggesting that α may be a way of identifying the PZC where the capacitance itself cannot.

The origin of the CPE is still heavily debated in the literature as it ultimately remains an empirical element and therefore its attribution to a physical phenomenon remains somewhat arbitrary. Nevertheless, some of the major previous theories have included (but are not limited to):[16,17]

1. Surface roughness-induced capacitive dispersion,[18−20]
2. Adsorption of trace impurities,[21]
3. An inhomogeneous current/potential distribution across the electrode due to geometry,[22−25] and/or EDL effects.[26−28]

The first of these propositions can be excluded here, as Pt(111) is atomically-flat, *i.e.*, surface roughness can be considered as negligible, and we have shown that increasing surface roughness by increasing the (110)-step density to (111)-terrace ratio leads to higher α values, not lower.[6] The second proposition is also unlikely in this context: although we previously demonstrated the presence of trace impurities in the $HClO_4$ stock electrolyte,[29] we find α actually increases with increasing electrolyte concentration (and hence higher impurity concentration), countering this argument. We thus argue that the third of these propositions (*i.e.*, CPE behavior being attributable to an inhomogeneous current/potential distribution across the electrode surface), is the most plausible explanation in this context, warranting further investigation.

Focusing on the third proposition, Newman originally put forward the idea that the CPE behavior can arise from a distributed or inhomogeneous capacitance and/or potential distribution across the electrode surface.[24,25] Newman's proposed analytical model assumes that current and potential distributions are governed solely by the resistance of the electrolyte solution to current flow, *i.e.*, by the primary current distribution. The inhomogeneity results from non-uniform current paths created by the electrode geometry and the finite conductivity of the electrolyte, even for an ideal blocking electrode. Newman's model refers to the simplified case of a planar inlaid disc electrode in an insulating shroud. This primary current density theory has been applied in analytical and numerical models to account for more complex geometries to study surface roughness and distributed capacitances.[30−32] Here the authors highlighted that while these heterogenous surface features create capacitance dispersion, this occurs at frequencies higher than those associated with the overall electrode geometry. To investigate the effect of other geometries, primary current distribution theory and numerical methods have been used to simulate an inlaid disc, a recessed disc and a rough electrode.[30,33] The concept of an inhomogeneous capacitance and/or potential distribution has been supported by experimental measurements both spectroscopically and electrochemically using recessed disc electrodes, but has so far been limited to polycrystalline materials.[34] However, these models based on Newman's work rely on the assumption that the electrode is ideally polarisable and do not consider the potential-dependent structure of the EDL.

To capture the potential-dependent structure of the EDL and incorporate key electrostatic phenomena, including ion migration and ohmic drop, the coupled Poisson-Nernst-Planck (PNP) equations are commonly solved either analytically or numerically. Numerical solutions offer the ability to consider the spatial and time-dependent variation in the ion concentrations and electric potential distributions, offering a dynamic description of the electrode-electrolyte interface under non-equilibrium conditions. The two-dimensional nature of double-layer charging is widely considered for nano and microelectrode voltammetry, where the electrode size is on the same length scale as the EDL.[35−39] Similar modeling approaches have been used to also model nanogap thin-layer cells which confines the electrolyte between two large planar electrodes within length scales comparable to the EDL,[40] making it important to spatially resolve the potential and ion distributions. In contrast, for larger macroscale systems, the electrode and cell geometry are typically neglected and assumed to be infinitely planar, allowing for the system to be reduced down to one dimension (1D).[41−45] To our knowledge, the coupling of the nanoscale of EDL charging to bulk two-dimensional macroscale (∼ mm) mass transport has not previously been explored. We will show that considering both length scales offers additional insight into the origin of the CPE behavior.

Using the model previously proposed by Newman, we find that any non-ideal charging can indeed be attributed to an inhomogeneous current distribution across the disc electrode surface, but it cannot explain the potential dependence of the experimental behavior. However, by solving the coupled PNP equations, we find that at potentials increasingly far from the PZC, the structural rearrangement of the EDL and the limited ion mobility (at low electrolyte concentrations) lead to non-uniform double layer charging across the electrode surface, which is amplified by the cell geometry. Conversely, at potentials close to the PZC, a marked decrease in α is observed experimentally. We attribute this to a potential-dependent electrowetting effect, which alters the electrolyte geometry in contact with the disc electrode in the hanging meniscus configuration, thereby modifying the local electric field. In summary, this work provides a more physical understanding of capacitance dispersion observed at potentials near the PZC for the Pt(111)/$HClO_4$ interface and, ultimately, has widespread implications for the single crystal community.

METHODS

Electrochemical Measurements

The electrochemical glassware cleaning procedure, cyclic voltammetry (CV) and EIS measurements as well as the ohmic drop compensation method used in this study followed protocols outlined previously.[16,29] A disc-type Pt(111) (diameter 3 mm, thickness 0.8 mm, MaTeck, 99.999%) was used as the working electrode for the majority of electrochemical measurements unless stated explicitly otherwise. Additional Pt(111) electrodes of varying dimensions were used (diameter 4 mm, thickness 2 mm, MaTeck, and diameter 6 mm, thickness 1 mm, MaTeck, 99.999%) for photographs of the edge

https://doi.org/10.1021/acselectrochem.5c00481
ACS Electrochem. 2026, 2, 693−704

wetting and comparison to a larger diameter electrode, respectively. All the potentials in this manuscript are reported versus the RHE scale for experimental measurements and have been appropriately ohmic drop-corrected. For further details and explanation of the choice of parameters in CV and EIS measurements, see ref 16. It should be noted that although explicit Kramers-Kronig consistency tests were not performed, the small AC perturbation amplitude, the absence of faradaic processes in the investigated potential window (i.e., the double-layer window), and the high internal consistency indicate that the EIS results are physically meaningful here. The experimental EIS data presented in this work were taken in random sequence of applied potential at least 3 times.

Finite Element Simulations

The model presented in this article builds upon previous work that fully accounts for ion migration, ohmic drop, and the structure of the potential-dependent EDL in 1D.[41] While the earlier model accounted for the coupled nature of faradaic and non-faradaic charging reactions during cyclic voltammetry, the model presented here focuses solely on the non-faradaic charging process. A schematic of the 2D axisymmetric geometry of the model is shown below in Figure 1.

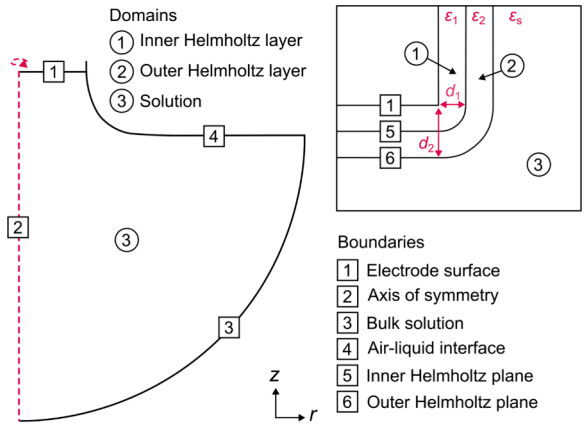

Figure 1. Schematic of the geometry used for the finite element simulation, with boundaries labeled with squares and the domains as circles. The inset shows a zoomed-in region at the edge of the electrode at ($r = r_0$) on the scale of the EDL.

Instead of considering an inlaid insulated disc,[46] a metal electrode of radius r_0 in a hanging meniscus electrode configuration is modeled to match the experimental single crystal measurements.[16,47,48] The charge is assumed to be fully delocalised across the metal electrode and is therefore described as a boundary, labeled as boundary 1 in Figure 1. The center of the electrode is positioned on the 2D axis of symmetry (boundary 2). The reference/counter electrode demarks the bulk solution (boundary 3) where the concentration and potential distributions are unperturbed. The air-liquid interface is labeled as boundary 4.

The EDL is described using a Gouy-Chapman-Stern (GCS) model where the compact Stern layer is further separated into the inner and outer Helmholtz layers, as depicted in the zoomed-in inset at the edge of the disc in Figure 1.[49] Following the methodology of the previous 1D model, including three layers separated by the inner Helmholtz plane (IHP) and outer Helmholtz plane (OHP). The IHP is located at d_1 = 0.29 nm (boundary 5) and the OHP at d_2 = 0.59 nm (boundary 6) from the electrode surface, with the latter marking the plane of closest approach for the solvated electrolyte ions. A three-state model is used to describe the dielectric properties of the EDL. Dielectric constants of 6 and 30 are used for the inner (domain 1) and outer (domain 2) Helmholtz layers, respectively.[49] The electrolyte solution beyond the OHP is denoted as domain 3, and it is assumed to have a constant dielectric constant ε_S = 78 at 298.15 K.[50] Note that the model assumes that all ions in the electrolyte domain are point charges.

The justification of the geometry of the meniscus for the model followed from experimental observations. To expose only the Pt(111) facet rather than the edges of the disc-shaped electrode, which are polycrystalline, we use a hanging meniscus configuration in experiments.[48] In the ideal case, the hanging meniscus configuration would resemble the configuration shown in Figure 2a (*i.e.*, a slightly concave shape). However, due to the overhead flow of argon maintained throughout the experiments to prevent oxygen permeation, the meniscus can break easily. Figure 2b depicts the more realistic hanging meniscus configuration used under our experimental conditions that remains stable for the duration of electrochemical measurements. As can be seen, this configuration results in edge wetting that is readily observed by eye (Figure 2b), meaning this effect must be accounted for when modeling the experimental results.

As discussed in more detail in Supporting Information (SI), File 1, a quantitative estimate for the height of this edge wetting observed in Figure 2b can be obtained by considering the ratio between the wetted and non-wetted parts of the edge of the crystal normalised to the thickness of the electrode. The results of this analysis show that the edge wetting height is relatively independent of the dimensions of the electrode itself and can be estimated to be ~200 μm, which was used as the value in the following modeling results. The width of the edge creep was arbitrarily estimated to be around 0.1% of the height of the edge creep (*i.e.*, 200 nm), which remains small enough to be considered a thin layer, but thick enough to avoid double-layer confinement effects under steady state conditions. In addition, we

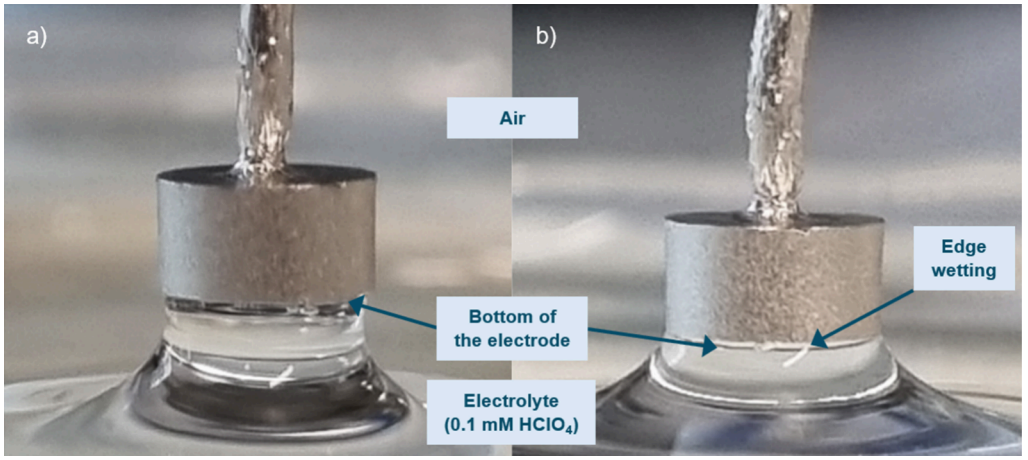

Figure 2. Images of a Pt(111) (diameter 4 mm, thickness 2 mm) disc electrode in 0.1 mM $HClO_4$ electrolyte in an (a) idealized hanging meniscus configuration with minimal edge wetting; (b) realistic hanging meniscus configuration with visible edge wetting. No potential applied.

https://doi.org/10.1021/acselectrochem.5c00481
ACS Electrochem. 2026, 2, 693−704

estimate the height, width and curvature of the meniscus, which means that our results are qualitative/semi-quantitative rather than quantitative.

To understand how the spatial and time dependence of double layer charging across the electrode-electrolyte interface creates an inhomogeneous capacitance and potential distribution, the Nernst-Planck equation was used to describe flux ($\mathbf{J}_i$) of the supporting electrolyte ions, H^+ and ClO_4^-, by diffusion and migration in the electrolyte solution:

$$\mathbf{J}_i = -D_i \nabla c_i - \frac{z_i F}{RT} D_i c_i \nabla \phi \tag{2}$$

where ϕ is the electric potential; D_i, c_i, and z_i are the diffusion coefficient, concentration, and electrostatic charge number of species i; and F, R and T are Faraday's constant, the ideal gas constant and temperature, respectively.

The Nernst-Planck equation was coupled to the Poisson equation to describe how the local concentration depends on the electric potential within the electrolyte solution:

$$\nabla^2 \phi = -\frac{F \sum z_i c_i}{\varepsilon_0 \varepsilon_s} \tag{3}$$

where ε_0 is the permittivity of free space and ε_S is the relative permittivity of water.

The simulations are performed by first solving the stationary steady-state (DC) concentration and electric potential distributions for a defined electrode potential, E_{DC}. A small harmonic (AC) perturbation, ΔE_{AC}, is then superimposed on the steady-state solution to simulate the system's response under AC conditions as described in eq 4:

$$E(t) = E_{DC} + \Delta E_{AC} \sin(\omega t) \tag{4}$$

where $E(t)$ is the time dependent applied potential to the electrode.

The model outputs are complex values with a phase and amplitude. Therefore, we analyze the phase and amplitude of the current response, while for the potential and concentration distributions, only the amplitude, $\Delta\phi$ and Δc_i, respectively, are extracted. These amplitudes correspond to the deviation of the total instantaneous response from the initial steady-state values. The simulations are computed at discrete frequencies, using 10 points per decade, to match the experimental sampling frequency. Further details of the geometry and mesh alongside the full corresponding set of boundary and domain equations are described in SI 2. The numerical simulations were performed using COMSOL Multiphysics version 6.2 using the transport of dilute species and electrostatic interfaces from the Electrochemistry module. In addition, the model report is also provided as a separate Supporting Information file, File 2.

RESULTS & DISCUSSION

In accordance with previous results, the capacitance measured in the double-layer window of the Pt(111)/$HClO_4$ interface (between 0.40−0.60 V vs. RHE) displays CPE behavior.[16] This can be readily observed from the Nyquist impedance plot (Figure 3a), where the experimental data (in this case taken at the PZC in 0.1 mM $HClO_4$) displays a frequency-dependent real impedance. The data deviates from the vertical line that would be expected for an ideal capacitor. Therefore, as shown in Figure 3a, a significantly better fit of the experimental data is obtained with a serial circuit containing a resistor (representing the solution resistance) and CPE electric equivalent circuit (RQ EEC) as opposed to an EEC consisting of a serial connection of a resistor and an ideal capacitor (RC EEC).

As discussed in the introduction, and irrespective of the presence of CPE behavior, the Pt(111)/$HClO_4$ interface deviates significantly from GC-theory as the GC-predicted capacitance minimum at the PZC, $C(Q)_{d,min}$, can only be directly observed in low electrolyte concentrations (0.1 mM,

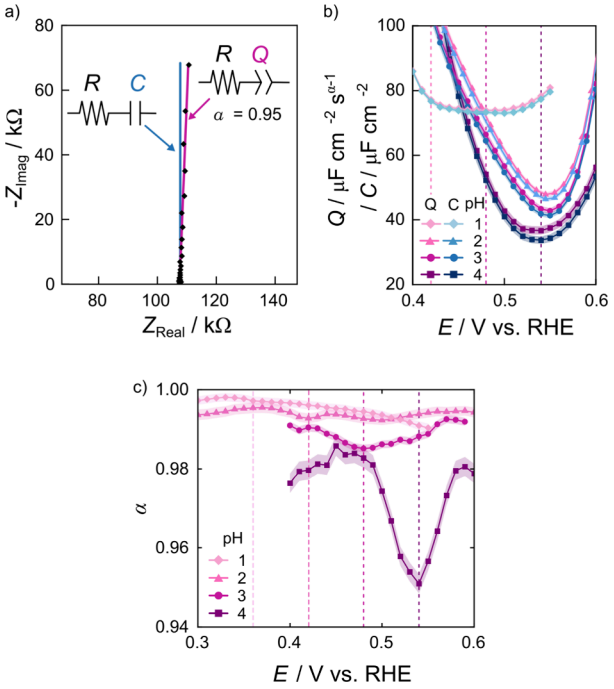

Figure 3. (a) Nyquist impedance plot at the PZC (0.54 V vs. RHE) in 0.1 mM $HClO_4$, where experimental data (black markers) is fitted with respective serial RQ (pink line) and RC (blue line) EECs (ΔE_{AC} = 5 mV, 1 kHz−0.5 Hz). (b) Capacitance values extracted from fitting EIS data for Pt(111) measured in x M $HClO_4$ with serial RQ and RC EECs, respectively shown at pH 1 (diamonds), pH 2 (triangles), pH 3 (circles), and pH 4 (squares). Vertical dotted lines indicate the PZC at the respective pH. (c) Corresponding CPE exponent values, α, for data shown in (b) when fitting with a serial RQ EEC. The data for pH 3 and pH 4 was previously reported in ref 16. Error bars are shown by the corresponding shaded regions, and all data points are the mean of at least three data sets, and the error is the population standard deviation for each point.

pH 4, Figure 3b). On the RHE scale, this GC-predicted $C(Q)_{d,min}$ should be observable at ∼0.48 and 0.42 V for pH's 3 and 2, respectively. As shown in Figure 3b, capacitance minima are indeed observable for these pH's in the double-layer window, but they appear at ∼0.55 V for both pH 3 and 2. We therefore argue that these capacitance minima do not correspond to the GC-predicted $C_{d,min}$ observed in pH 4 as they appear at the incorrect potential (in comparison to their respective expected PZCs).[51]

Interestingly, however, a minimum in the CPE exponent, α, can be observed at the expected PZC for pH 3 at 0.48 V and also at pH 2 a small local minimum was observed at the expected PZC of 0.42 V (Figure 3c). This suggests that α is sensitive to the PZC where the capacitance is not. Importantly, the extent of CPE behavior, *i.e.*, how far the average value of α is from 1, increases with decreasing electrolyte concentration. This electrolyte concentration dependence is also reflected in the closer agreement observable between the capacitance values obtained when fitting the EIS response with either an RQ or RC EEC, respectively, at lower pH's/higher electrolyte concentrations (Figure 3b).

As discussed in the introduction, we exclude that the CPE behavior observed is attributable to the specific adsorption of trace impurities,[21] as α increases with increasing electrolyte concentration (Figure 3c). This trend contradicts what would be expected if the effect were due to trace impurity adsorption,

https://doi.org/10.1021/acselectrochem.5c00481
ACS Electrochem. 2026, 2, 693−704

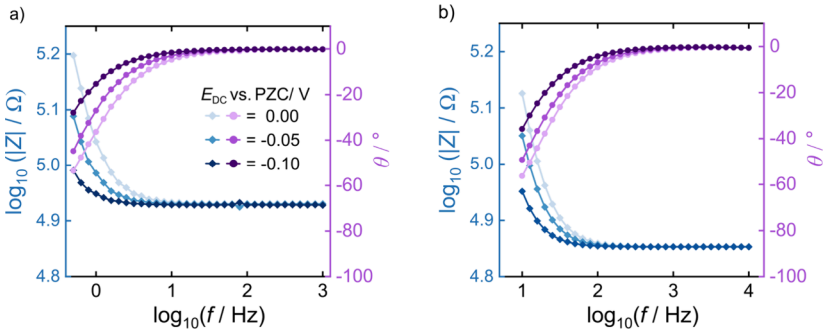

Figure 4. (a) Experimental Bode impedance plot at different potentials from the PZC in 0.1 mM $HClO_4$ (1 kHz − 0.5 Hz); (b) PNP-modeled Bode impedance plot for the same conditions (10 kHz − 10 Hz). The applied E_{DC} potentials are shown at 0.00 (light), −0.05 (medium), and −0.10 V (dark) vs. PZC. |Z| is shown in blue (diamonds, left axis) and θ in purple (circles, right axis). Model parameters: ΔE_{AC} = 5 mV, D_{H+} = 9.3 × 10^{-5} cm^2 s^{-1}, D_{ClO4-} = 1.8 × 10^{-5} cm^2 s^{-1}, c_{elec}* = 0.1 mM, r_0 = 1.5 mm, ε_1 = 6, ε_2 = 30, ε_S = 78, z_{H+} = +1, z_{ClO4-} = −1. All other geometry parameters are defined in Table S3, SI 2.

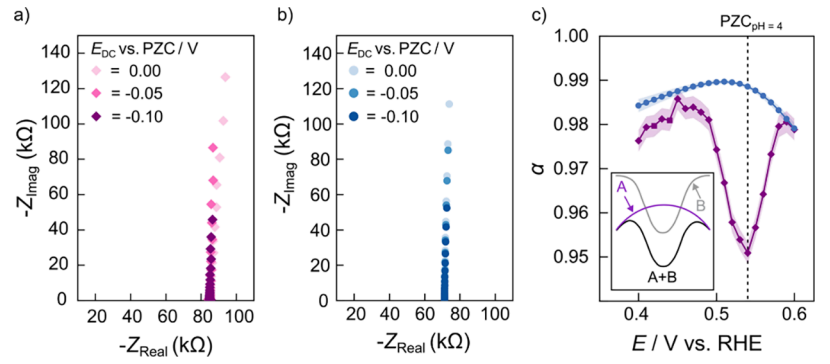

Figure 5. Nyquist plots obtained from (a) experiments (pink) in 0.1 mM $HClO_4$ (1 kHz − 0.5 Hz) and (b) PNP simulations (blue) under the same conditions (10 kHz − 10 Hz) at 0.00 (pale), -0.05 (medium) and -0.10 V vs. PZC (dark). (c) Plot of α for the experimental (pink, diamonds) results previously shown in Figure 3c and simulated (blue, circles) results extracted. The potential axis corresponds to E_{DC} assuming PZC = 0.30 V + 0.06·pH = 0.54 V vs. RHE (pH 4). Error bars for the PNP simulations, shown as a blue shaded region, correspond to the standard error of the linear regression slope. The inset shows a schematic of two regimes: A (purple), which is the CPE behavior arising from a static meniscus geometry and B (gray) the CPE behavior arising from a second potential-dependent effect. All other parameters are as listed in Figure 4.

as higher electrolyte concentrations would typically lead to increased impurity levels, thereby enhancing (rather than diminishing) the observed CPE behavior.[29] Furthermore, given that the EIS measurements presented here were carried out in random order of applied potential (see Experimental methods section), the CPE profile observed here (*i.e.*, the change in α as a function of potential) cannot be attributed to time effects but are intrinsic to the system. Such time effects could result from either meniscus evaporation resulting from overhead Ar flow during measurement, or from impurity accumulation over time. Instead, an inhomogeneous current/potential distribution across the electrode surface is the most likely cause of CPE behavior in this context, as previously shown and modeled by Newman, and later expanded upon by other authors.[23−25,33,52] Initially we used Newman's primary current distribution model to simulate the impedance response of the hanging meniscus geometry discussed in Figure 1 and Figure 2, in order to assess how closely this model approximates the experimental trends in Figure 3. In Figure S6, SI 3 we show the Nyquist and Bode plots for the hanging meniscus geometry in 0.1 mM $HClO_4$ using experimentally measured conductivity and capacitance of 2.8 mS m^{-1} and 37 μF cm^{-2}, respectively. Unlike in Figure 3a, the Nyquist plot in Figure S6a displays no observable CPE behavior, and the α value extracted is 0.993, *i.e.*, very close to an ideal capacitor where α = 1. It is assumed in Newman's model that the surface charge is perfectly screened by a double layer which has a negligible thickness. This assumption would suggest Newman's model is only appropriate to describe high (>0.1 M) concentrations of supporting electrolyte at the PZC and is insufficient to describe the CPE behavior of the Pt(111)/$HClO_4$ interface at low electrolyte concentrations relevant to the present context.

To capture the potential-dependence of the double layer, we instead solve the PNP equations at a range of steady state potentials, E_{DC}, on either side of the PZC, to explicitly account for the structure of the EDL in the finite element model. Results are shown in Figure 4, where the Bode impedance plot from experiments in 0.1 M $HClO_4$ (Figure 4a) is compared with the finite element simulations (Figure 4b). Here, the impedance magnitude (|Z|) and phase angle (θ), shown in blue and purple respectively, are both plotted at the PZC (light shades), -0.05 V vs. PZC (medium shades) and -0.1 V vs. PZC (dark shades). We explore here only potentials negative of the PZC, as there is a broader potential range in the experimental data to compare to in 0.1 mM $HClO_4$ at negative potentials of the PZC. Both plots show a potential dependence at the low end of the frequency range: as the E_{DC} moves away from the PZC, |Z| and |θ| both become smaller. The region in Figure 4 where the impedance response depends on E_{DC} corresponds to the CPE region, characterized by a mixed resistive and capacitive behavior. Above ∼500 Hz in the simulation, the response is dominated by solution resistance, which is

https://doi.org/10.1021/acselectrochem.5c00481
ACS Electrochem. 2026, 2, 693−704

independent of potential. In SI 4, we discuss the impact of using the PNP equations across an extended frequency range of 1 mHz to 10 MHz which is beyond those used in experiments and show the potential dependence of the Bode plot across this range in Figure S9.

It should be noted that it is only possible to replicate the same behavior observed experimentally by shifting the frequency range plotted from 0.5 Hz − 1 kHz to 10 Hz − 10 kHz for the simulations. This is carried out to ensure we are capturing the physical processes behind the CPE behavior and provide a more faithful comparison between experiments and simulations. Discussion of how this frequency range was chosen is discussed in more detail in SI 5. This shift is likely due to the measured capacitance of Pt(111), which is an order of magnitude greater (~32-37 μF cm^{-2}) than the capacitance predicted by a GCS model (~2−3 μF cm^{-2}), even at dilute concentrations of 0.1 mM.[16] Previous research has attributed the larger capacitance of Pt(111) to weak ion-surface interactions, which are not captured in this model.[7,53] Furthermore, we cannot fully define the exact geometry of the edge-wetting region, which can, as we will discuss later, have a marked effect on the α values extracted. For reference, all the parameters used, and their source can be found in Table S3. The parameters put into the model are based on values extracted from the literature without any further modification to improve the fit of the simulation.

The experimentally obtained Nyquist plots (Figure 5a) match reasonably to the simulated ones (Figure 5b) for the imaginary component of the impedance (Z_{Imag}). The simulation matches the behavior of the experiments, appearing as a tilted straight line in this frequency range. However, the high-frequency intercept on the real impedance axis, which corresponds to the uncompensated solution resistance, is lower for the simulated (71 kΩ) compared to the experimental (85 kΩ) results.

From the simulated data, α is calculated using the method presented by Orazem *et al.*:[54]

$$\log_{10}(|Z_{Imag}|) = -\alpha \log_{10}(\omega) + c \quad (5)$$

so that when plotting the magnitude of the imaginary impedance, $|Z_{Imag}|$, against the angular frequency, ω, the slope is equal to -α on a logarithmic scale. However, in both the experiments and simulations, the slope is not constant as a function of frequency, therefore, we extract α only over a range where the response is linear. Examples of the fits can be found in SI 5 and all values in Figure 5 are extracted from fits with an $R^2 \geq 0.9998$.

Figure 5c shows the potential-dependent values of α extracted from both the experiments in 0.1 mM $HClO_4$ and the PNP simulations. Here, the α values from the simulations display a maximum instead of the experimentally obtained minimum (Figure 3c) at the PZC, albeit that in the simulation this maximum is slightly offset by -0.03 V with respect to the PZC. This implies that by accounting for EDL charging effects using the PNP model, α would be expected to decrease as we increase the potential away from the PZC (±50 mV). Interestingly, this effect captures to some extent the CPE behavior observed experimentally at potentials further from the PZC, especially for 0.48−0.42 V (Figure 5c), where a general decrease in α is observable with increasing potential away from the PZC. Nevertheless, these simulations reveal that the current model does not capture the marked minimum in α observable at the PZC in experiments. This suggests that there is a second potential-dependent phenomenon that dominates in this potential window, leading to a decrease in α at the PZC not captured by the current model. To distinguish the two potential regions in which we propose these two effects respectively dominate, we refer to the schematic shown in the inset of Figure 5c: regions A (purple curve) and B (gray curve). Here, region A refers to the "background" CPE behavior we would expect for a static hanging meniscus configuration geometry (and can be accounted for with the current model), and region B refers to a secondary effect that dominates at potentials close to the PZC, respectively. As discussed in more detail below, we attribute region B to potential-dependent electrowetting, which alters the geometry of the edge wetting up the sides of the disk electrode and consequently modifies the local electric field distribution as a function of potential. The overall CPE behavior observed experimentally is then a convolution of these two effects (*i.e.*, A + B, black curve, Figure 5c).

To better understand region A, *i.e.*, why the capacitance behavior becomes more non-ideal with increasing potentials away from the PZC, we examine how the spatial distribution of the electric potential varies across different applied potentials, E_{DC}. Since we are evaluating the harmonic perturbation, we plot and discuss the amplitude of the electric potential, $\Delta\phi$. In Figure 6 the $\Delta\phi$ distribution is plotted as a contour plot for E_{DC} values of (a) 0.00 V, (b) -0.05 V and (c) -0.10 V vs. PZC at 10 Hz, where potential-dependent CPE behavior is observed in the simulations. Each band corresponds to a 0.5 mV increment in $\Delta\phi$, with pale yellow indicating values between 0 and 0.5 mV, while dark purple corresponds to values between

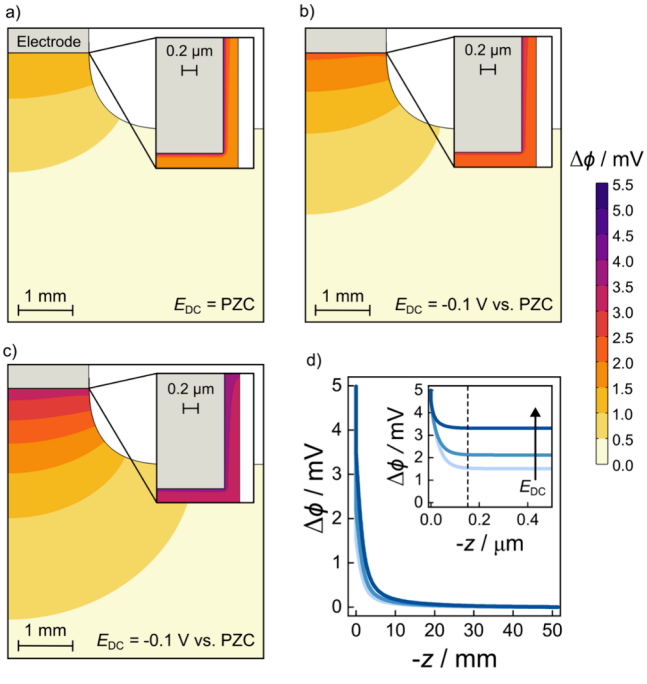

Figure 6. Contour plots of the $\Delta\phi$ distribution at 10 Hz across a 0.1 mM $HClO_4$ electrolyte solution at (a) 0.00, (b) −0.05, and (c) −0.1 V vs. PZC, where each band corresponds to a 0.5 mV change. Insets show a zoomed-in section at the edge of the disc. (d) Plot of the corresponding $\Delta\phi$ along the z axis going away from the center of the electrode surface (r = 0) at 0.00 (light), −0.05 (mid), and −0.10 V vs. PZC (dark), with an inset zoomed in to 0.5 μm from the electrode surface. All other parameters are as listed in Figure 4.

https://doi.org/10.1021/acselectrochem.5c00481
ACS Electrochem. 2026, 2, 693−704

5.0 and 5.5 mV. Note this is larger than the 5 mV harmonic perturbation used in experiments and simulations due to the mass transport effects in the thin wetted edge. The bands transition from being widely spaced and radially distributed in bulk solution to becoming tightly spaced and nearly planar close to the electrode surface, following the electrode surface boundary, as illustrated in the insets. Although the hanging meniscus electrode configuration limits the radial accessibility of the surface to current-carrying ions (similar to a recessed disc electrode configuration),[55] the edge of the electrode remains radially accessible. The difference in accessibility across the electrode surface to current carrying ions, creates the non-uniform current and/or potential distribution across the electrode surface proposed by Newman as shown in Figure S12 and discussed in more detail in SI 6.[25]

Additionally, the spatial distribution of $\Delta\phi$ across the cell is dependent on E_{DC}. At the PZC, as shown in Figure 6**a**, more than half of the applied 5 mV perturbation drops within a few hundreds of nanometres from the electrode surface. In contrast, at the more negative potential of -0.10 V vs. PZC shown in Figure 6c, a greater proportion is dropped across the bulk electrolyte solution. This dependence on the E_{DC} is more clearly illustrated in Figure 6d, where the $\Delta\phi$ distribution is shown only along the z axis moving perpendicularly away from the center of the electrode surface (0, 0) for E_{DC} values of 0.00 V (pale blue), -0.05 V (mid blue) and -0.10 V (dark blue) vs. PZC. The inset of Figure 6d also shows the data on the scale of the diffuse layer of the EDL, where the dashed line corresponds to approximately the edge of the EDL, defined here as 5 times the Debye length λ_D,

$$\lambda_D^{-1} = \sqrt{\frac{F^2 \sum_i z_i^2 C_i^*}{\varepsilon_S \varepsilon_0 RT}} \tag{6}$$

5 times the Debye length marks the effective distance where over 99% of the electric field is screened by the redistribution of ions under equilibrium conditions.

At 10 Hz, the ions are unable to redistribute to fully screen the surface charge of the electrode, causing the potential drop to extend beyond the EDL ($>5\lambda_D$) at all three potentials. As a result, the structure of the double layer deviates from equilibrium at this frequency. This difference with E_{DC} arises from the potential-dependent structure of the EDL established during the initial steady-state solution, prior to the application of the harmonic perturbation. At the PZC, the small AC perturbation induces near symmetrical ion redistribution. On the other hand, at potentials far away from the PZC, the interface is already highly polarised due to the large asymmetric accumulation/depletion of ions, creating a strong electric field across the EDL. Because the steady-state electric field is already strong and the ion-distribution asymmetric, the small AC perturbation only slightly modifies the existing electric field, resulting in a limited rearrangement of ions. With a limited rearrangement of ions near the interface, more of the potential drop is distributed across the bulk solution.

The asymmetric potential dependence of α extracted in Figure 5c either side of the PZC arises from the difference in the diffusion coefficients of H^+ (9.3×10^{-5} cm^2 s^{-1}) and ClO_4^- (1.8×10^{-5} cm^2 s^{-1}) ions,[56] accounted for in the PNP model. This difference effects each ion's electrical mobility (u_i) via the Nernst−Einstein relation.

$$u_i = \frac{|z_i| F D_i}{RT} \tag{7}$$

As the $\Delta\phi$ distribution extends further into the bulk at potentials away from the PZC, migration-driven flux also becomes increasingly dominant, amplifying the effect of the asymmetric diffusion coefficients. In addition, according to the Nernst-Planck equation, migration scales not only with electrical mobility, but also with the bulk electrolyte concentration (eq 1).

This difference in transport properties causes the system to respond differently depending on the sign of the applied potential relative to the PZC, leading to the skewed response in Figure 5c. At potentials negative of the PZC, the more mobile H^+ ions are locally accumulated and can respond more quickly to the perturbation in potential by diffusion and migration than the ClO_4^- ions at an equal but opposite (positive) potential relative to the PZC. This leads to a lag in the electrode charging and less accumulation at the surface of the electrode. This effect is enhanced at the electrode edges, where radial mass transport and the stronger local field gradients amplify the non-uniform and asymmetric charging behavior. The asymmetry in the potential dependence of α can be removed by setting the diffusion coefficient of H^+ and ClO_4^- to be equal. Adjusting both to 5.5×10^{-5} cm^2 s^{-1} (the mean of their original values), preserves the bulk electrolyte conductivity of 4.2 mS m^{-1} for 0.1 mM $HClO_4$, as shown in Figure 7.

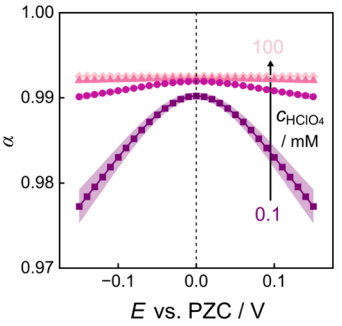

Figure 7. Plot of α extracted from simulations vs. E_{DC}, when D_{H+} = D_{ClO4-} = 5.5×10^{-5} cm^2 s^{-1} with varying concentrations x M $HClO_4$. The electrolyte concentration is set at 0.1 (squares), 1 (circles), 10 (triangles), and 100 mM (diamonds). All other parameters are as listed in Figure 4.

On the other hand, as shown in Figure 7 increasing the electrolyte concentration from 0.1 mM (dark purple) to 100 mM (light pink) increases α at potentials away from the PZC. At increasing electrolyte concentrations, the diffuse layer is more compact, and ions can screen the charge on the metal electrode more effectively. This trend is supported by the corresponding simulated Bode plots for concentrations of 0.1−100 mM $HClO_4$ (pH 4−1) shown in Figures S13 and SI7, where the potential-dependent deviation in the θ and $|Z|$ diminishes with increasing concentrations of $HClO_4$. Importantly, however, α never reaches the ideal value of 1, but it plateaus at ∼0.99 for this cell and electrode geometry. This persistent deviation from ideal capacitance behavior is attributed to the inhomogeneous potential and current distributions created by the non-uniformly accessible cell geometry.[25]

https://doi.org/10.1021/acselectrochem.5c00481
ACS Electrochem. 2026, 2, 693−704

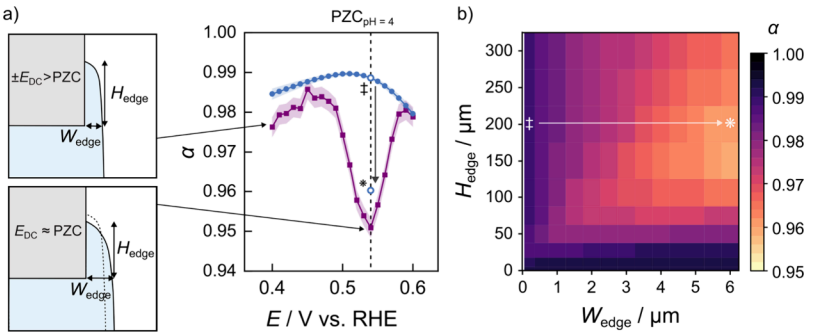

Figure 8. (a) Plot of the data in Figure 5c overlaid with the additional point (hollow circles) corresponding to the α value extracted for an edge creep height of 200 μm and width of 6 μm. All other parameters are as listed in Figure 4. (b) Color plot of α for a matrix of height (H_{edge}) and width (W_{edge}) values for the geometry of the edge creep at the PZC.

In summary, the decrease in α at potentials away from the PZC (Figure 5c, region A) arises from the interplay between the structure of the electrode-electrolyte interface and the local electric field distribution shaped by the cell geometry. The hanging meniscus configuration promotes a near-planar current path near the electrode surface, reducing the non-uniform current and potential distribution across the electrode surface that would be observed for a more radially accessible in-laid disk, as proposed by Newman.[25] However, unlike Newman's model which assumes the EDL is an ideal Helmholtz capacitor, in the PNP model the structure of the EDL is dependent on E_{DC} as well as the diffusion coefficients, bulk concentrations and electrostatic charge of the ions present. At potentials far from the PZC, the interface is highly polarised, and the AC perturbation of the EIS measurements leads to non-uniform charging due to the finite transport of ions. While the hanging meniscus configuration limits radial effects, the edge of the electrode remains more accessible than the center, amplifying the effect of the asymmetry in mass transport of ions at potentials away from the PZC. The cell configuration results in the CPE behavior persisting even at high electrolyte concentrations, though the effect is very small.

However, as discussed above, the PNP model does not account for the minimum in α at the PZC observed experimentally (*i.e.*, region B, Figure 5c). To further understand the origin of this secondary effect, one could think of the following (though not exhaustive) plausible explanations: 1) changes in the interfacial dielectric properties of the solvent;[57] 2) specific adsorption at the PZC;[58] and 3) electrowetting. The first two of these explanations are unlikely in this context, as the frequencies at which these effects become significant fall outside the range of our experimental conditions. Specifically, since anion adsorption from ClO_4^- (or from trace impurities in the electrolyte) is negligible in this context, the most probable adsorbate in this potential window would be H_2O. However, the characteristic frequencies associated with H_2O adsorption, as well as with interfacial dielectric responses, are expected to lie in the GHz range,[59] which lie far beyond our accessible experimental frequency window (as discussed in more detail in ref 16, the upper frequency limit is limited to 1 kHz in 0.1 mM $HClO_4$ due to the interference of a high-frequency artifact).

Instead, we propose that the latter of these propositions, namely that there is an electrowetting effect that will impact the potential-dependent geometry of the wetted edge (*i.e.*, as shown in Figure 2b) is the most likely cause of a minimum in α at the PZC. Electrowetting itself has previously been well-studied on carbon electrodes, revealing that at the PZC the least wetting should be observed, whereas with increasing potential away from the electrode (regardless of being positive or negative), a symmetric increase in wetting would be expected.[60] This electrowetting would have a marked impact on the geometry of the wetted edge, where an increase in wetting should result in a lower contact angle, ultimately resulting in a thinner and taller wetted edge geometry (top left schematic, Figure 8a). On the other hand, at the PZC, the least wetting is expected and therefore the contact angle should increase and the wetted edge geometry should become wider and slightly shorter (bottom left schematic, Figure 8a). Given the significant edge wetting we observe in the realistic hanging meniscus configuration (Figure 2b), it is reasonable to assume that the effect of such an electrowetting would indeed be marked.

To explore this potential-dependent wetting, we model different edge geometries at the PZC and extract the corresponding α using the same method discussed previously for Figure 5c, where an edge height, H_{edge}, of 200 μm and a width, W_{edge}, of 0.2 μm (0.1% of the height) were used. Here, we change the height from H_{edge} = 0 μm (no creep) to 300 μm (creep) as well as the width from W_{edge} = 0.2 μm (thin) to 6 μm (thick) and all fits had an $R^2 > 0.9998$. This range of heights is based on the optical images discussed in Figure 2 and SI 1. The choice of a small change in width is based on the optical images, which showed no observable change with E_{DC}. In Figure 8b, α is plotted as a color map with the dark purple corresponding to where $0.998 < \alpha < 1.000$, *i.e.*, more ideal capacitive behavior, and yellow when $0.950 < \alpha < 0.952$, *i.e.*, less ideal capacitive behavior. For the parameter space explored, there is no significant effect of the edge width on α, if the edge height stays below ~25 μm. As soon as this threshold value is exceeded, an increase in wetted edge width significantly increases α. This has a strong effect on our investigated system, where the experimentally obtained creep height was H_{edge} = 200 μm.

We would expect that both the height and the width of the wetted edge region will change with potential. For example, Figure 8a shows that if the width of the edge is indeed increased by more than an order of magnitude from 0.2 μm (the double dagger symbol) to 6 μm (the star symbol), a significant decrease in α is observed, causing a similar minimum in the α to that experimentally observed, as highlighted in Figure 8b. In contrast, changes in edge height must be in the range of several tens of micrometers, making us conclude that changes in the edge width have a more pronounced effect on α than the variations in the height of

https://doi.org/10.1021/acselectrochem.5c00481
ACS Electrochem. 2026, 2, 693−704

the edge creep. Nevertheless, for a different initial meniscus geometry, variations in the height of the edge creep may be more significant.

These results reveal the importance of including the wetted edge in the model, as even a small change in the wetted edge geometry is sufficient to alter the local electric field and contribute to a decrease in α. Nevertheless, the edge may also contribute to the voltammetric signal, as the edges of single-crystalline disc electrodes are typically polycrystalline. As is now generally well accepted in the platinum electrochemistry community, all facets other than (111) exhibit no adsorbate-free potential windows in $HClO_4$, *i.e.*, some adsorption should occur on the wetted edge sites where it would not for the (111) facet in the double-layer window.[3−6] Additionally, the PZC of the edge sites likely differs from that of the (111) facet, which could also contribute to the observed CPE behavior.[61−63]

To evaluate whether the electrochemistry at the edge contributes significantly to the experimentally obtained signal, we carried out the same EIS measurements on a semi-submerged Pt(111) electrode in 0.1 mM $HClO_4$ (*i.e.*, still meniscus-like, however, edges were wetted significantly more, see Figure S14). As shown in Figure S15, the average values of α decrease by ∼0.1 in the semi-submerged meniscus configuration compared to the realistic hanging meniscus configuration. Given that the sides of a single crystal disc electrode are polycrystalline in nature, this decrease in α for the semi-submerged Pt(111) electrode compared to the usual hanging meniscus configuration is consistent with generally lower α values measured previously for polycrystalline Pt electrodes at similar potentials.[63,64] In the semi-submerged configuration more of the polycrystalline Pt edge sites are wetted relative to the Pt(111) facet which is further confirmed by the increasingly polycrystalline nature of the blank CV, Figure S17. However, it is important to note that while the average α values decrease, the relative trend, *i.e.*, the depth of the minimum in α near the PZC (region B, Figure 5c) relative to the background α values at potentials further from the PZC (region A, Figure 5c), remains the same between both meniscus configurations. These observations suggest that adsorption at the edges is unlikely to be the major reason for the minimum in α we observe at the PZC as adsorption leads to a decrease in α at all potentials, but does not seem to affect CPE behavior at the PZC specifically. Furthermore, the PZC of a polycrystalline Pt electrode is different to that of Pt(111) due to constituting a combination of different facets as well as adsorption of water-dissociated species on the lower-coordinated facets (*i.e.*, hydrogen and hydroxyl species).[65] Therefore, the fact that a minimum in α is still observed at the PZC of Pt(111) suggests that the inherent nature of electrowetting changing the potential drop across the edge-wetted region is the key factor governing CPE behavior in this context rather than the chemistry of the wetted edge site itself. The latter effect would only lead to an overall decrease in the α value. This is further confirmed by a decrease in α for a correspondingly larger diameter Pt(111) electrode (see Figure S16), which has a smaller edge-to-surface ratio, ultimately suggesting that the minimum in α at the PZC is more likely attributable to an inhomogeneous current/potential distribution that changes as a function of edge geometry due to wetting rather than due to electrochemical differences between the edge and the surface. See SI 8 for more details.

CONCLUSIONS & OUTLOOK

Despite its status as a benchmark system in electrochemistry, the Pt(111)/$HClO_4$ interface displays pronounced deviations from ideal capacitive behavior. Using the hanging meniscus configuration for single crystal electrochemistry and EIS, we reveal two distinct regimes of CPE behavior at potentials close to the PZC: 1) a general decrease in the CPE exponent, α, at potentials further from the PZC and, 2) a pronounced minimum in α at the PZC.

By combining experimental measurements with numerical solutions to the PNP equations in 2D, we demonstrate that the CPE behavior observed throughout the double-layer window arises from inhomogeneous charging of the EDL. This originates from capacitance and/or potential dispersion across the electrode surface. For a static geometry, we find that as a function of potential, α should reach a maximum approximately at the PZC, depending on the symmetry of the diffusion coefficients, and decrease with increasing potential away from the PZC. Therefore, the model captures the CPE behavior observed experimentally at potentials further away from the PZC (*i.e.*, the first regime). To account for the second regime, namely a minimum in α at the PZC, we argue that the geometry of the wetted part of a non-trivial proportion of edge sites due to the hanging meniscus configuration changes as a function of potential, leading to a different distribution of current/potential across the electrode surface itself. Ideally, the frequency-dependent information could be used to derive more information about interfacial properties, like the PZC. However, we showed that the frequency dispersion is not only influenced by the potential-dependent structure of the double layer, but also by the 2D geometry of the experimental setup.

These findings underscore the critical role of the electrode and cell geometry in interpreting CPE behavior. Our results further reveal that the edge of the electrode is an active three-phase boundary, the influence of which must be considered when evaluating interfacial properties near the PZC. We also establish that as the electrolyte concentration decreases, the diffuse layer increasingly dominates over the capacitive behavior of the Helmholtz layer, making mass transport effects more significant, a phenomenon only captured through the PNP model. This work therefore offers a more complete understanding of inhomogeneous capacitance distribution near the PZC. The model introduced in this work can also be applied to understand the time-dependent behavior of confined electrochemical double layers in nanoporous geometries.

While this study resolves several key ambiguities, it also opens new questions, particularly regarding the direct experimental confirmation of electrowetting effects and edge-related phenomena near the PZC. More specifically, an interesting follow-up study would be to gain an understanding of how the surface tension relates to the shape of the electrowetting film as the electrowetting tail would be maximised at the PZC due to maximal surface tension. Continued investigation in this direction will be crucial for extending our understanding to more complex electrode architectures and for refining models of electrochemical interfaces in systems where geometric confinement and interfacial heterogeneity play significant roles. Ultimately, the insights gained here are broadly applicable to the single-crystal electrochemistry community and provide a solid foundation for future studies of interfacial phenomena in model systems.

https://doi.org/10.1021/acselectrochem.5c00481
ACS Electrochem. 2026, 2, 693−704

■ ASSOCIATED CONTENT

Data Availability Statement

Data will be made available in a public repository upon publication.

Supporting Information

The Supporting Information is available free of charge at https://pubs.acs.org/doi/10.1021/acselectrochem.5c00481.

File 1: Justification of meniscus height estimation; details of the finite-element model implemented in COMSOL Multiphysics; discussion of the primary current distribution model; frequency dependence of the PNP model; details of the method for calculating the CPE exponent; inhomogeneous potential and capacitance distribution; concentration dependence of the CPE behavior; additional experimental data (PDF)

File 2: COMSOL-generated report corresponding to the finite element model (PDF)

■ AUTHOR INFORMATION

Corresponding Author

Marc T.M. Koper − *Leiden Institute of Chemistry, Leiden University, Leiden 2333 CC, the Netherlands;* orcid.org/0000-0001-6777-4594; Email: m.koper@lic.leidenuniv.nl

Authors

Katherine J. Levey − *Leiden Institute of Chemistry, Leiden University, Leiden 2333 CC, the Netherlands;* orcid.org/0000-0003-4843-2710

Nicci L. Fröhlich − *Leiden Institute of Chemistry, Leiden University, Leiden 2333 CC, the Netherlands;* orcid.org/0009-0004-4655-6415

Steffen Hardt − *Leiden Institute of Chemistry, Leiden University, Leiden 2333 CC, the Netherlands*

Lucas B.T. de Kam − *Leiden Institute of Chemistry, Leiden University, Leiden 2333 CC, the Netherlands;* orcid.org/0009-0000-3943-6619

Complete contact information is available at: https://pubs.acs.org/10.1021/acselectrochem.5c00481

Author Contributions

[+]K.J.L. and N.L.F. contributed equally.

Notes

The authors declare no competing financial interest.

■ ACKNOWLEDGMENTS

We thank Dr Julia Fernández Vidal and Dr Marco Schönig for helpful discussion. K.J.L. and M.T.M.K. acknowledge the partial financial support from the Dutch Research Council (Spinoza Award) and from the European Union's Horizon Europe Research and Innovation programme, project DECODE under Grant Agreement No 101135537. Views and opinions expressed are, however, those of the author(s) only and do not necessarily reflect those of the European Union. Neither the European Union nor the granting authority can be held responsible for them. N.L.F. and M.T.M.K. received funding from the European Research Council (ERC) (advanced grant no. 101019998 "FRUMKIN"). S.H. acknowledges funding from the European Union's Horizon Europe 2022 research and innovation program under the Marie Skłodowska-Curie grant agreement (no.101104814).

■ REFERENCES

(1) Koper, M. T. M. Blank Voltammetry of Hexagonal Surfaces of Pt-Group Metal Electrodes: Comparison to Density Functional Theory Calculations and Ultra-High Vacuum Experiments on Water Dissociation. *Electrochim Acta* **2011**, *56* (28), 10645−10651.

(2) Pajkossy, T.; Kolb, D. M. Double Layer Capacitance of Pt(111) Single Crystal Electrodes. *Electrochim Acta* **2001**, *46* (20), 3063−3071.

(3) McCrum, I. T.; Chen, X.; Schwarz, K. A.; Janik, M. J.; Koper, M. T. M. Effect of Step Density and Orientation on the Apparent PH Dependence of Hydrogen and Hydroxide Adsorption on Stepped Platinum Surfaces. *J. Phys. Chem. C* **2018**, *122* (29), 16756−16764.

(4) Rizo, R.; Fernández-Vidal, J.; Hardwick, L. J.; Attard, G. A.; Vidal-Iglesias, F. J.; Climent, V.; Herrero, E.; Feliu, J. M. Investigating the Presence of Adsorbed Species on Pt Steps at Low Potentials. *Nat. Commun.* **2022**, *13* (1), 2550.

(5) Rizo, R.; Chico-Mesa, L.; Arán-Ais, R. M.; Climent, V.; Herrero, E.; Feliu, J. M. Analysis of the OH Coverage on Low-Coordinated Pt Sites at Low Potentials. *ACS Electrochemistry* **2025**, *1* (3), 351−359.

(6) Fröhlich, N. L.; Liu, J.; Ojha, K.; Hagopian, A.; Doblhoff-Dier, K.; Koper, M. T. M. A Comprehensive Model for the Electric Double Layer of Stepped Platinum Electrodes. *Accepted Nat. Chem.* **2025**.

(7) Ojha, K.; Doblhoff-Dier, K.; Koper, M. T. M. Double-Layer Structure of the Pt(111)-Aqueous Electrolyte. *Proc. Natl. Acad. Sci. U. S. A.* **2022**, *119* (3), No. e2116016119.

(8) Ojha, K.; Arulmozhi, N.; Aranzales, D.; Koper, M. T. M. Double Layer at the Pt(111)−Aqueous Electrolyte Interface: Potential of Zero Charge and Anomalous Gouy−Chapman Screening. *Angew. Chem., Int. Ed.* **2020**, *59* (2), 711−715.

(9) Schmickler, W.; Santos, E. *Interfacial Electrochemistry*, 2nd ed.; Springer: Berlin, Germany, 2010.

(10) Grahame, D. C. The Electrical Double Layer and the Theory of Electrocapillarity. *Chem. Rev.* **1947**, *41* (3), 441−501.

(11) Climent, V.; Coles, B. A.; Compton, R. G. Coulostatic Potential Transients Induced by Laser Heating of a Pt(111) Single-Crystal Electrode in Aqueous Acid Solutions. Rate of Hydrogen Adsorption and Potential of Maximum Entropy. *J. Phys. Chem. B* **2002**, *106* (23), 5988−5996.

(12) Martínez-Hincapié, R.; Climent, V.; Feliu, J. M. Peroxodisulfate Reduction as a Probe to Interfacial Charge. *Electrochem commun* **2018**, *88*, 43−46.

(13) Sebastián, P.; Martínez-Hincapié, R.; Climent, V.; Feliu, J. M. Study of the Pt (111) | Electrolyte Interface in the Region Close to Neutral PH Solutions by the Laser Induced Temperature Jump Technique. *Electrochim Acta* **2017**, *228*, 667−676.

(14) Weaver, M. J. Potentials of Zero Charge for Platinum(111)−Aqueous Interfaces: A Combined Assessment from In-Situ and Ultrahigh-Vacuum Measurements. *Langmuir* **1998**, *14* (14), 3932−3936.

(15) Rizo, R.; Sitta, E.; Herrero, E.; Climent, V.; Feliu, J. M. Towards the Understanding of the Interfacial PH Scale at Pt(111) Electrodes. *Electrochim Acta* **2015**, *162*, 138−145.

(16) Fröhlich, N. L.; Eggebeen, J. J. J.; Koper, M. T. M. Measurement of the Double-Layer Capacitance of Pt(111) in Acidic Conditions near the Potential of Zero Charge. *Electrochim Acta* **2024**, *494*, No. 144456.

(17) Lasia, A. The Origin of the Constant Phase Element. *J. Phys. Chem. Lett.* **2022**, *13* (2), 580−589.

(18) Kerner, Z.; Pajkossy, T. Impedance of Rough Capacitive Electrodes: The Role of Surface Disorder. *Journal of Electroanalytical Chemistry* **1998**, *448* (1), 139−142.

(19) Bidóia, E. D.; Bulhões, L. O. S.; Rocha-Filho, R. C. Pt/HClO4 Interface CPE: Influence of Surface Roughness and Electrolyte Concentration. *Electrochim Acta* **1994**, *39* (5), 763−769.

(20) Scheider, W. Theory of the Frequency Dispersion of Electrode Polarization. Topology of Networks with Fractional Power Frequency Dependence. *J. Phys. Chem.* **1975**, *79* (2), 127−136.

(21) Martin, M. H.; Lasia, A. Influence of Experimental Factors on the Constant Phase Element Behavior of Pt Electrodes. *Electrochim Acta* **2011**, *56* (23), 8058−8068.
(22) Hirschorn, B.; Orazem, M. E.; Tribollet, B.; Vivier, V.; Frateur, I.; Musiani, M. Determination of Effective Capacitance and Film Thickness from Constant-Phase-Element Parameters. *Electrochim Acta* **2010**, *55* (21), 6218−6227.
(23) Huang, V. M.-W.; Vivier, V.; Orazem, M. E.; Pébère, N.; Tribollet, B. The Apparent Constant-Phase-Element Behavior of a Disk electrode with Faradaic Reactions. *J. Electrochem. Soc.* **2007**, *154* (2), C99.
(24) Newman, J. Frequency Dispersion in Capacity Measurements at a Disk. *J. Electrochem. Soc.* **1970**, *117* (2), 198.
(25) Newman, J. Current Distribution on a Rotating Disk below the Limiting. *J. Electrochem. Soc.* **1966**, *113* (12), 1235.
(26) Pajkossy, T.; Jurczakowski, R. Electrochemical Impedance Spectroscopy in Interfacial Studies. *Curr. Opin Electrochem* **2017**, *1* (1), 53−58.
(27) Singh, M. B.; Kant, R. Debye−Falkenhagen Dynamics of Electric Double Layer in Presence of Electrode Heterogeneities. *Journal of Electroanalytical Chemistry* **2013**, *704*, 197−207.
(28) van der Geest, M. E.; Dangerfield, N. J.; Harrington, D. A. An Ac Voltammetry Study of Pt Oxide Growth. *Journal of Electroanalytical Chemistry* **1997**, *420* (1), 89−100.
(29) Fröhlich, N.; Fernández-Vidal, J.; Mascaró, F. V.; Shih, A. J.; Luo, M.; Koper, M. T. M. Effect of Trace Impurities in Perchloric Acid on Blank Voltammetry of Pt(111). *Electrochim Acta* **2023**, *466*, No. 143035.
(30) Alexander, C. L.; Tribollet, B.; Orazem, M. E. Contribution of Surface Distributions to Constant-Phase-Element (CPE) Behavior: 1. Influence of Roughness. *Electrochim Acta* **2015**, *173*, 416−424.
(31) Alexander, C. L.; Tribollet, B.; Orazem, M. E. Contribution of Surface Distributions to Constant-Phase-Element (CPE) Behavior: 2. Capacitance. *Electrochim Acta* **2016**, *188*, 566−573.
(32) Alexander, C. L.; Tribollet, B.; Orazem, M. E. Influence of Micrometric-Scale Electrode Heterogeneity on Electrochemical Impedance Spectroscopy. *Electrochim Acta* **2016**, *201*, 374−379.
(33) Huang, V. M. W.; Vivier, V.; Orazem, M. E.; Pébère, N.; Tribollet, B. The Apparent Constant-Phase-Element Behavior of an Ideally Blocking Electrode. *J. Electrochem. Soc.* **2007**, *154* (2), C81.
(34) Niu, B.; Xie, R.-C.; Ren, B.; Long, Y.-T.; Wang, W. Radially Distributed Charging Time Constants at an Electrode-Solution Interface. *Nat. Commun.* **2024**, *15* (1), 5633.
(35) Fan, L.; Liu, Y.; Xiong, J.; White, H. S.; Chen, S. Electron-Transfer Kinetics and Electric Double Layer Effects in Nanometer-Wide Thin-Layer Cells. *ACS Nano* **2014**, *8* (10), 10426−10436.
(36) Liu, Y.; He, R.; Zhang, Q.; Chen, S. Theory of Electrochemistry for Nanometer-Sized Disk Electrodes. *J. Phys. Chem. C* **2010**, *114* (24), 10812−10822.
(37) Norton, J. D.; White, H. S.; Feldberg, S. W. Effect of the Electrical Double Layer on Voltammetry At. *J. Phys. Chem.* **1990**, *94* (17), 6772−6780.
(38) Smith, C. P.; White, H. S. Theory of the Voltammetric Response of Electrodes of Submicron. Violation of Electroneutrality in the Presence of excess Supporting Electrolyte. *Anal. Chem.* **1993**, *65* (23), 3343−3353.
(39) Dickinson, E. J. F.; Compton, R. G. Diffuse Double Layer at Nanoelectrodes. *J. Phys. Chem. C Nanomater. Interfaces* **2009**, *113* (41), 17585−17589.
(40) Chen, Q.; McKelvey, K.; Edwards, M. A.; White, H. S. Redox Cycling in Nanogap Electrochemical Cells. The Role of Electrostatics in Determining the Cell Response. *J. Phys. Chem. C* **2016**, *120* (31), 17251−17260.
(41) Levey, K. J.; Edwards, M. A.; White, H. S.; Macpherson, J. V. Simulation of the Cyclic Voltammetric Response of an Outer-Sphere Redox Species with Inclusion of Electrical Double Layer Structure and Ohmic Potential Drop. *Phys. Chem. Chem. Phys.* **2023**, *25* (11), 7832−7846.
(42) Pendergast, A. D.; White, H. S. Double-Layer Inhibition of Peroxydisulfate Reduction at Mercury Ultramicroelectrodes. A Quantitative Analysis of the Frumkin Effect Including Molecular Transport and Long-Range Electron Transfer. *J. Phys. Chem. C* **2023**, *127* (23), 11283−11297.
(43) He, R.; Chen, S.; Yang, F.; Wu, B. Dynamic Diffuse Double-Layer Model for the Electrochemistry of Nanometer-Sized Electrodes. *J. Phys. Chem. B* **2006**, *110* (7), 3262−3270.
(44) Streeter, I.; Compton, R. G. Numerical Simulation of Potential Step Chronoamperometry at Low Concentrations of Supporting Electrolyte. *J. Phys. Chem. C* **2008**, *112* (35), 13716−13728.
(45) Wang, H.; Thiele, A.; Pilon, L. Simulations of Cyclic Voltammetry for Electric Double Layers in Asymmetric Electrolytes: A Generalized Modified Poisson−Nernst−Planck Model. *J. Phys. Chem. C* **2013**, *117* (36), 18286−18297.
(46) Wu, S.-L.; Orazem, M. E.; Tribollet, B.; Vivier, V. The Influence of Coupled Faradaic and Charging Currents on Impedance Spectroscopy. *Electrochim Acta* **2014**, *131*, 3−12.
(47) Villullas, H. M.; Lopez Teijelo, M. Meniscus Shape and Lateral Wetting at the Hanging Meniscus Rotating Disc (HMRD) Electrode. *J. Appl. Electrochem* **1996**, *26* (3), 353−359.
(48) Dickertmann, D.; Koppitz, F. D.; Schultze, J. W. Eine Methode Zum Ausschluss von Randeffekten Bei Elektrochemischen Messungen an Einkristallen: Test Anhand Der Adsorptionssysteme Ag/Pb2+ Und Au/Cu2+. *Electrochim Acta* **1976**, *21* (11), 967−971.
(49) Bockris, J. O.; Devanathan, M. A. V.; Müller, K. On the Structure of Charged Interfaces. *Proc. R Soc. Lond A Math Phys. Sci.* **1963**, *274* (1356), 55−79.
(50) Malmberg, C. G.; Maryott, A. A. Dielectric Constant of Water from 0 0 to 100 0 C. *J. Res. Natl. Bur. Stand.* **1956**, *56* (I), 1.
(51) Fröhlich, N. L.; Koper, M. T. M. Progress and Pitfalls in Measuring the Double-Layer Capacitance of Platinum Electrodes. *Curr. Opin Electrochem* **2025**, *53*, No. 101727.
(52) Huang, V. M.-W.; Vivier, V.; Frateur, I.; Orazem, M. E.; Tribollet, B. The Global and Local Impedance Response of a Blocking Disk Electrode with Local Constant-Phase-Element Behavior. *J. Electrochem Soc.* **2007**, *154* (2), C89.
(53) Schmickler, W. The Effect of Weak Adsorption on the Double Layer Capacitance. *ChemElectroChem.* **2021**, *8* (22), 4218−4222.
(54) Orazem, M. E.; Pébère, N.; Tribollet, B. Enhanced Graphical Representation of Electrochemical Impedance Data. *J. Electrochem Soc.* **2006**, *153* (4), B129.
(55) Frateur, I.; Huang, V. M.-W.; Orazem, M. E.; Pébère, N.; Tribollet, B.; Vivier, V. Local Electrochemical Impedance Spectroscopy: Considerations about the Cell Geometry. *Electrochim Acta* **2008**, *53* (25), 7386−7395.
(56) *CRC Handbook of Chemistry and Physics* , 97th ed.; Lide, D. R., Bruno, T. J., Eds.; CRC Press: Boca Raton, 2016.
(57) Cole, K. S.; Cole, R. H. Dispersion and Absorption in Dielectrics I. Alternating Current Characteristics. *J. Chem. Phys.* **1941**, *9* (4), 341−351.
(58) Climent, V.; Attard, G. A.; Feliu, J. M. Potential of Zero Charge of Platinum Stepped Surfaces: A Combined Approach of CO Charge Displacement and N2O Reduction. *Journal of Electroanalytical Chemistry* **2002**, *532* (1), 67−74.
(59) Limmer, D. T.; Willard, A. P.; Madden, P. A.; Chandler, D. Water Exchange at a Hydrated Platinum Electrode Is Rare and Collective. *J. Phys. Chem. C* **2015**, *119* (42), 24016−24024.
(60) Papaderakis, A. A.; Leketas, M.; Wei, Z.; Hwang, I.; Carbone, P.; Juel, A.; Dryfe, R. A. W. Electrowetting of Carbon-Based Materials for Advanced Electrochemical Technologies. *ChemElectroChem.* **2024**, *11* (10), No. e202400143.
(61) Climent, V.; Gómez, R.; Feliu, J. M. Effect of Increasing Amount of Steps on the Potential of Zero Total Charge of Pt(111) Electrodes. *Electrochim Acta* **1999**, *45* (4), 629−637.
(62) Clavilier, J.; Albalat, R.; Gomez, R.; Orts, J. M.; Feliu, J. M.; Aldaz, A. Study of the Charge Displacement at Constant Potential during CO Adsorption on Pt(110) and Pt(111) Electrodes in Contact

https://doi.org/10.1021/acselectrochem.5c00481
ACS Electrochem. 2026, 2, 693−704

with a Perchloric Acid Solution. *Journal of Electroanalytical Chemistry* **1992**, *330* (1), 489−497.
(63) Fröhlich, N. L.; Sjö, H.; Mascaró, F. V.; Koper, M. T. M. Correlating Surface Structure and Electrochemical Properties of Polycrystalline Platinum Electrodes. *Electrochim Acta* **2026**, *548*, No. 147977.
(64) Bidóia, E.D.; Bulhões, L.O.S.; Rocha-Filho, R.C. Pt/$HClO_4$ Interface *CPE*: Influence of Surface Roughness and Electrolyte Concentration. *Electrochim. Acta.* **1994**, *39* (5), 763−769.
(65) Rizo, R.; Herrero, E.; Climent, V.; Feliu, J. M. On the Nature of Adsorbed Species on Platinum Single-Crystal Electrodes. *Curr. Opin. Electrochem.* **2023**, *38*, 101240.

https://doi.org/10.1021/acselectrochem.5c00481
ACS Electrochem. 2026, 2, 693−704